# Madden–Julian Oscillation analog and intraseasonal variability in a multicloud model above the equator

Andrew J. Majda[†‡], Samuel N. Stechmann[†], and Boualem Khouider[§]

[†]Courant Institute of Mathematical Sciences and Center for Atmosphere and Ocean Sciences, New York University, New York, NY 10012; and [§]Department of Mathematics and Statistics, University of Victoria, Victoria, BC, Canada V8W 2Y2

The Madden–Julian Oscillation (MJO) is the dominant component of tropical intraseasonal variability, and a theory explaining its structure and successful numerical simulation remains a major challenge. A successful model for the MJO should have a propagation speed of 4–7 m/s predicted by theory; a wavenumber-2 or -3 structure for the planetary-scale, low-frequency envelope with distinct active and inactive phases of deep convection; an intermittent turbulent chaotic multiscale structure within the planetary envelope involving embedded westward- and eastward-propagating deep convection events; and qualitative features of the low-frequency envelope from the observational record regarding, e.g., its zonal flow structure and heating. Here, such an MJO analog is produced by using the recent multicloud model of Khouider and Majda in an appropriate intraseasonal parameter regime for flows above the equator so that rotation is ignored. Key features of the multicloud model are (*i*) systematic low-level moisture convergence with retained conservation of vertically integrated moist static energy, and (*ii*) the use of three cumulus cloud types (congestus, stratiform, and deep convective) together with their differing vertical heating structures. Besides all of the above structure in the MJO analog waves, there are accurate predictions of the phase speed from linear theory and transitions from weak, regular MJO analog waves to strong, multiscale MJO analog waves as climatological parameters vary. With all of this structure in a simplified context, these models should be useful for MJO predictability studies in a fashion akin to the Lorenz 96 model for the midlatitude atmosphere.

coherent planetary intraseasonal variability | multiscale structure | intermittency in convection | nonlinear analog model

The dominant component of intraseasonal variability in the Tropics is the 40- to 50-day tropical intraseasonal oscillation, often called the Madden–Julian Oscillation (MJO) after its discoverers (1). In the troposphere, the MJO is an equatorial planetary-scale wave envelope of complex multiscale convective processes that begins as a standing wave in the Indian Ocean and propagates across the western Pacific at a speed of $\approx 5$ m·s$^{-1}$ (2–5). The planetary-scale circulation anomalies associated with the MJO significantly affect monsoon development and intraseasonal predictability in midlatitudes and the development of the El Niño southern oscillation in the Pacific Ocean, which is one of the most important components of seasonal prediction (6, 7). Present-day computer general circulation models typically poorly represent the MJO (8, 9). One conjectured reason for the poor performance of general circulation models is the inadequate treatment across multiple spatial scales of the interaction of the hierarchy of organized structures that generate the MJO as their envelope.

There have been a large number of theories attempting to explain the MJO through a specific linearized mechanism, such as evaporation–wind feedback (10, 11), boundary layer frictional convective convergence (12), stochastic linearized convection (13), radiation instability (14), and the planetary-scale linear response to moving heat sources (15). Moncrieff (16) recently developed an interesting phenomenological nonlinear theory for

the upscale transport of momentum from equatorial mesoscales [$O$ (300 km)] to planetary scales and applied this theory to explain the "MJO-like" structure in recent "superparameterization" computer simulations (17, 18) with a scale gap (no resolution at all) on scales between 200 and 1,200 km. Multiscale diagnostic models with prescribed MJO phase speed have been used to isolate key features of the nonlinear dynamics that create the observed structure of the MJO envelope (19–21). Despite all of these interesting contributions, the problem of explaining the MJO has recently been called the search for the Holy Grail of tropical atmospheric dynamics (14). Here we contribute to this search.

Analysis of observational data from TOGA-COARE (Tropical Ocean Global Atmosphere Coupled Ocean Atmosphere Response Experiment) provides a revealing look into the multicloud and multiscale structure of convection in the Tropics (22) and, in particular, the MJO (23–25). These observations reveal a central role of three cloud types above the boundary layer in the MJO: lower-middle troposphere congestus cloud decks that moisten and precondition the lower troposphere in the initial phase, followed by deep convection and a trailing wake of upper troposphere stratiform clouds (23, 25). Observations also reveal the complex multiscale structure within the propagating large-scale envelope of the MJO; the embedded smaller scale features include westward-propagating two-day waves, eastward-propagating superclusters or convectively coupled Kelvin waves (26, 27), and smaller-scale squall line clusters that typically propagate westward (2, 25). The analysis of observations of the MJO (23, 25, 28) also reveals a complex vertical structure in the MJO envelope with a vertical tilt involving a low-level westerly onset region below easterlies, strong westerlies in the deep convective region, and strongest westerlies aloft in the lower-middle troposphere in the stratiform region; there is also a leading vertical dipole potential temperature anomaly in the troposphere with warmer temperature anomalies above cooler temperature anomalies and leading low-level moistening.

Building on earlier work (29, 30), Khouider and Majda (31–34) recently developed a systematic multicloud model convective parameterization highlighting the nonlinear dynamical role of the three cloud types, congestus, stratiform, and deep convective clouds, and their different vertical structures: a deep convective heating mode and a second vertical mode with low-level heating and cooling corresponding to congestus and stratiform clouds. Detailed linear stability analysis (31, 34) and nonlinear simulations (32, 33) reveal a mechanism for large-scale

APPLIED MATHEMATICS

**Table 1. Multicloud model parameter values**

| Parameter | Description | Value |
|---|---|---|
| $\tau_{conv}$ | Deep convective adjustment time | 12 h |
| $\tau_s$ | Stratiform heating adjustment time | 7 days |
| $\tau_c$ | Congestus heating adjustment time | 7 days |
| $a_0$ | Inverse buoyancy time scale of convective parameterization | 12 |
| $\bar{Q}$ | Background moisture stratification | 1.0 |
| $\bar{\theta}_{eb} - \bar{\theta}_{em}$ | RCE value of the difference in equivalent potential temperature between the boundary layer and middle troposphere | 12 K |
| $\tilde{\lambda}$ | Second baroclinic relative contribution to the moisture convergence associated with the background moisture gradient | 0.6 |
| $\tau_u$ | Momentum drag relaxation time | 150 days |
| $\tau_\theta$ | Newtonian cooling relaxation time | 100 days |
| $C_d$ | Boundary layer turbulent momentum friction coefficient | $1.0 \times 10^{-5}$ |

The values listed are used unless otherwise noted. Parameters not listed here take the same values as in the standard case of ref. 31.

instability of moist gravity waves. The multicloud model reproduces key features of the observational record for convectively coupled Kelvin waves or two-day waves (26, 35, 36), including phase speeds in the range of 15–20 m·s$^{-1}$, vertical wave tilts, and anomalous vertical dipoles in potential temperature.

## The Strategy for Producing an MJO Analog

The strategy in this paper is to exploit the observed statistical self-similarity of tropical convection (37) and study the multicloud models for superclusters in a parameter regime appropriate for intraseasonal variability.

Key parameters of the multicloud model (31, 34) are the bulk climatological parameters: $\bar{\theta}_{eb} - \bar{\theta}_{em}$, the mean equivalent potential temperature difference between the boundary layer and lower-middle troposphere; and $\bar{Q}$, the bulk low-level moisture gradient. Key parameters in the convective parameterization are the time scales for multicloud dynamics: congestus time scale $\tau_c$, deep convective time scale $\tau_{conv}$, and stratiform time scale $\tau_s$. In earlier work (31–34), the parameters $\tau_c$, $\tau_{conv}$, and $\tau_s$ were used in the range of 1–3 h to parameterize the unresolved effects of convective wave packets from smaller scales on the equatorial synoptic supercluster scales. Here, by exploiting the observed statistical self-similarity of tropical convection (37), the multicloud models are studied with the parameters $\tau_c$, $\tau_{conv}$, and $\tau_s$ in an intraseasonal planetary regime:

$$\tau_{conv} = O(12 \text{ h}), \quad \tau_c, \tau_s = O(7 \text{ days}). \qquad [1]$$

Note that the time scale for $\tau_{conv}$ in Eq. 1 is consistent with the current observational estimates for large-scale consumption of convective available potential energy (38). In addition, a current observational study of low-level moistening and congestus cloud development in the MJO suggests a time scale of 1–2 weeks for these processes, consistent with Eq. 1 (W. K.-M. Lau, personal communication). Of course, the long lags in Eq. 1 with forcing and damping are surrogates for complex multiscale processes not resolved directly in the present model, which is why the terminology "MJO analog" is used throughout the paper.

A realistic analog MJO wave should have all of the following features:

A. An actual propagation speed of 4–7 m·s$^{-1}$ predicted by theory.

B. A wavenumber-2 or -3 structure for the low-frequency planetary-scale envelope with distinct active and inactive phases of deep convection.

C. An intermittent turbulent chaotic multiscale structure within the wave envelope involving embedded westward- and eastward-propagating deep convection events.

D. Qualitative features of the low-frequency averaged planetary-scale envelope from the observational record in terms of, e.g., vertical structure of heating and westerly wind burst.

$$[2]$$

At the present time, only the MJO-like wave produced by Grabowski (17, 18) in numerical simulations has most of these features. In this paper, MJO analog waves with all four of the key features listed in Eq. 2 are produced and analyzed in the multicloud model in a suitable parameter regime with a constant sea surface temperature.

The next step in the strategy is to vary the regime of climatological parameters $\bar{\theta}_{eb} - \bar{\theta}_{em}$ and $\bar{Q}$ in linear stability analysis with all other parameters in the multicloud models fixed at their standard values as in refs. 31, 32, and 34. The key regime for the climatological parameters occurs when linear stability analysis predicts items A and B in Eq. 2, and simultaneously

A linearly unstable band at large scales with wavenumbers $1 \leq k \leq O(10)$ and growth rates of approximately $(40 \text{ days})^{-1}$ to $(20 \text{ days})^{-1}$. $\qquad [3]$

The plentiful band of large-scale unstable wavenumbers is necessary to produce item C of Eq. 2 in the nonlinear simulations as shown below. The robust regime of climatological parameters is explored below both through linear theory and nonlinear simulations.

It is worthwhile to mention here that the present models produce realistic MJO analog waves satisfying the conditions in item C of Eq. 2 within the multicloud model where the only nonlinear mechanisms are

A. Low-level moisture advection and

B. Nonlinear switches for deep and congestus convection.

$$[4]$$

In particular, MJO analog waves satisfying item C of Eq. 2 are produced within the multicloud model without the following mechanisms: (*i*) wind-induced surface heat exchange (10, 11), (*ii*) boundary layer frictional moisture convergence, (*iii*) explicit effects of rotation through the beta effect, (*iv*) active radiation, (*v*) active atmosphere/ocean coupling, and (*vi*) upscale eddy flux
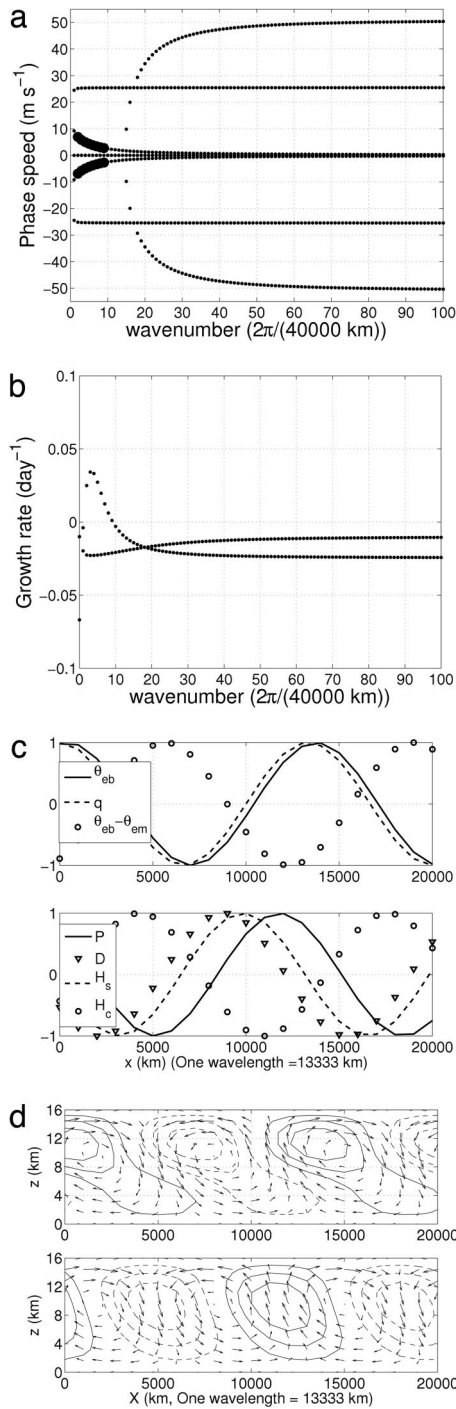
**Fig. 1.** Linear stability analysis with the multicloud model using parameter values shown in Table 1. (*a*) Phase speeds (in meters per second), with stable modes plotted as small dots and unstable modes as big dots. (*b*) Growth rates (per day). The most unstable mode is a wavenumber-3 mode, with a growth rate of 0.034 day$^{-1}$ and a phase speed of $\pm 5.8$ m·s$^{-1}$. (*c*) Phase relationships for the eastward-moving, unstable wavenumber-3 mode, with magnitudes of all variables normalized to 1. (*d*) Velocity field (*U, W*) with contours of potential temperature (*Upper*) and contours of total convective heating (*Lower*) for the eastward-moving, unstable wavenumber-3 mode. The total convective heating is the sum of congestus, stratiform, and deep convective heating.

divergences of momentum. As mentioned above, these mechanisms are advocated in the literature as being important for the MJO, and they can be incorporated in various ways in the present MJO analog models in the future to give further physical insight.
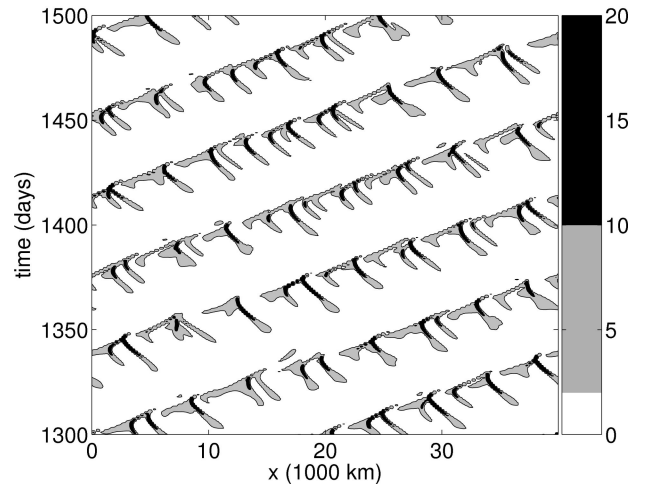


**Fig. 2.** Contour plot of the deep convective heating $P(x, t)$ from a numerical simulation of the multicloud model using the parameter values in Table 1. Heating values of >2 K per day are shaded in gray, and values of >10 K per day are shaded in black.

## The Multicloud Model

The multicloud model (31–34) is given by

$$\begin{cases} \partial_t u_1 - \partial_x \theta_1 = -C_d(u_0)u_1 - u_1/\tau_u \\ \partial_t \theta_1 - \partial_x u_1 = P - R_1 \end{cases} \quad [5a]$$

$$\begin{cases} \partial_t u_2 - \partial_x \theta_2 = -C_d(u_0)u_2 - u_2/\tau_u \\ \partial_t \theta_2 - \partial_x u_2/4 = H_c - H_s - R_2 \end{cases} \quad [5b]$$

$$\begin{cases} \partial_t \theta_{eb} = (E - D)/h_b \\ \partial_t q = -(2\sqrt{2}/\pi)P + D/H_T \\ \qquad - \partial_x[(q + \tilde{Q})u_1 + (\tilde{\alpha}q + \tilde{\lambda}\tilde{Q})u_2] \end{cases} \quad [5c]$$

$$\begin{cases} \dfrac{\partial H_s}{\partial t} = \dfrac{1}{\tau_s}(\alpha_s P - H_s) \\ \dfrac{\partial H_c}{\partial t} = \dfrac{1}{\tau_c}\left(\alpha_c \dfrac{\Lambda - \Lambda^* D}{1 - \Lambda^* H_T} - H_c\right) \end{cases} \quad [5d]$$

The diagnostic variables are $u_j$ and $\theta_j$, the zonal velocity and potential temperature of the $j$th baroclinic mode; $\theta_{eb}$, the equivalent potential temperature of the boundary layer; $q$, the vertically averaged water vapor content; $H_s$, the stratiform heating; and $H_c$, the congestus heating. The source terms are $R_j$, the radiative cooling of the $j$th baroclinic mode; $P$, the deep convective heating; $E$, the evaporation; and $D$, the downdrafts. The deep convective heating $P$ has one factor $P_0$ involving a Betts–Miller-type closure with an adjustment time $\tau_{conv}$, which is a key parameter in the multicloud model:

$$P = \frac{1 - \Lambda}{1 - \Lambda^*} P_0, \quad P_0 = \frac{1}{\tau_{conv}}(a_1\theta_{eb} + a_2(q - \hat{q}) - \alpha_0(\theta_1 + \gamma_2\theta_2))^+$$

$$[6]$$

where $\Lambda$ is a nonlinear switch that takes values between $\Lambda^*$ and 1, and $f^+ = \max(f, 0)$. See ref. 31 for the form of the other source terms.

The multicloud model has been introduced, analyzed, and utilized as a model for convectively coupled gravity waves (31–34). In the present study, the model parameters are frozen
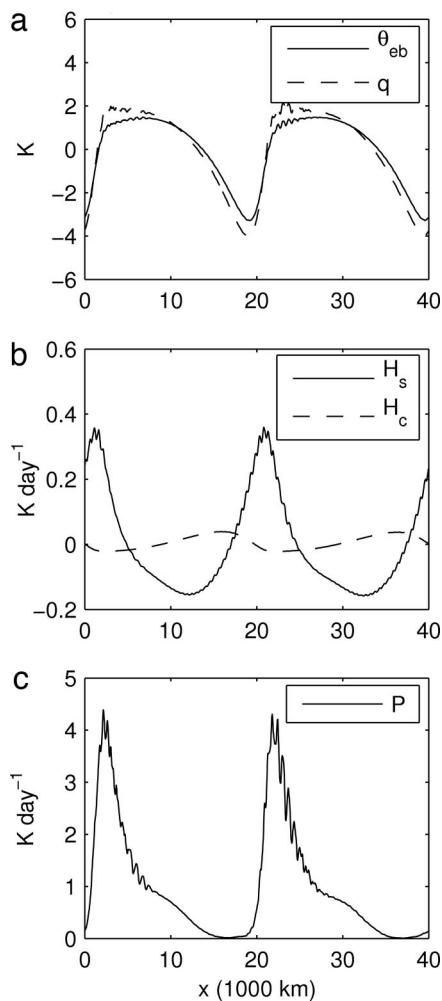
**Fig. 3.** Moving average of model variables for the simulation in Fig. 2. (*a*) Equivalent potential temperature of the boundary layer, $\theta_{eb}$, and vertically averaged water vapor, $q$. (*b*) Stratiform heating, $H_s$, and congestus heating, $H_c$. (*c*) Deep convective heating, $P$. The moving average was taken in a reference frame moving with the planetary-scale envelope of deep convection in Fig. 2, at 6.1 m·s$^{-1}$. RCE values have been removed from $\theta_{eb}$, $q$, $H_s$, and $H_c$ for this plot.

to the standard values used in earlier work (31) except those listed in Table 1. Eq. 5 is written in nondimensional units, where the equatorial Rossby deformation radius, $L_e \approx 1,500$ km, is the length scale; the first baroclinic dry gravity wave speed, $c \approx 50$ m·s$^{-1}$, is the velocity scale; $T = L_e/c \approx 8$ h is the associated time scale; and the dry static stratification, $\bar{\alpha} = H_T N^2 \theta_0/(\pi g) \approx 15$ K, is the temperature unit scale. Vertical velocities are nondimensionalized by the scale ratio factor $c \cdot H_T/(\pi L_e)$, where $H_T \approx 16$ km is the height of the tropical troposphere.

The dynamical core of the multicloud convective parameterization consists of two coupled shallow water systems: a direct heating mode in Eq. 5a forced by heating from the phase change from deep penetrative clouds and a second baroclinic mode in Eq. 5b forced by both stratiform heating and congestus heating. In Eq. 5, $u_1$ and $u_2$ represent the first and second baroclinic velocities with vertical profiles $G(z) = \sqrt{2}\,\cos(\pi z/H_T)$ and $G(2z) = \sqrt{2}\,\cos(2\pi z/H_T)$, respectively, whereas $\theta_1$ and $\theta_2$ are the corresponding potential temperature components with the vertical profiles $G'(z) = \sqrt{2}\,\sin(\pi z/H_T)$ and $2G'(2z) = 2\sqrt{2}\,\sin(2\pi z/H_T)$, respectively. Therefore, the total velocity field is approximated by
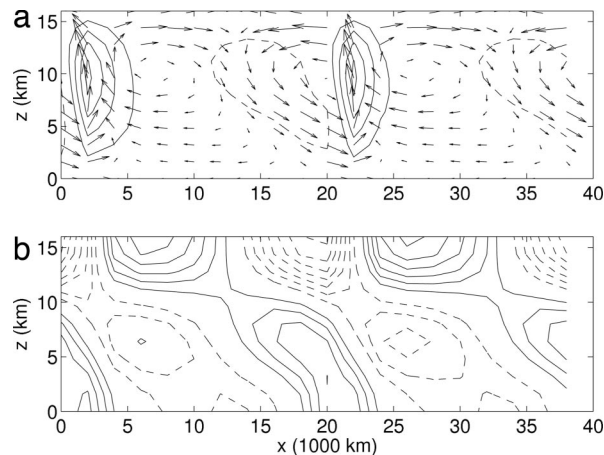


**Fig. 4.** Moving average (as in Fig. 3) of model variables with their vertical structures. Dashed contours are for negative values, and solid contours are for positive values, with the zero contour removed. (*a*) Velocity field (*U*, *W*) with contours of total convective heating (congestus, stratiform, and deep convective heating combined). The contour interval is 1 K per day. RCE values of *P*, $H_s$, and $H_c$ were removed for this plot. (*b*) Contours of horizontal velocity, *U*, with contour interval of 1 m·s$^{-1}$.

$$U \approx G(z)u_1 + G(2z)u_2 \text{ and}$$
$$W \approx -(H_T/\pi)[G'(z)\partial_x u_1 + G'(2z)\partial_x u_2/2], \quad [7]$$

where $U$ is the horizontal velocity, $W$ is the vertical velocity, and the total potential temperature is given approximately by $\Theta \approx z + G'(z)\theta_1 + 2G'(2z)\theta_2$.

Unless otherwise noted, all numerical experiments reported below use the same numerical methods used in earlier studies (32, 33), with a horizontal mesh spacing $\Delta x = 40$ km on a periodic domain of 40,000 km mimicking the troposphere above the equator.

## MJO Analog Waves in the Multicloud Model

Here, we follow the strategy outlined above, with a uniform background sea surface temperature given by the constant $\theta_{eb}^*$, and produce MJO analog waves with the features in Eq. 2 in a suitable parameter regime for the multicloud model.

**MJO Analog Waves: The Basic Example.** Here the values $\bar{Q} = 1.0$ and $\bar{\theta}_{eb} - \bar{\theta}_{em} = 12$ K are used for the climatological parameters in the multicloud model. Consistent with the discussion below Eq. 1, the multicloud time scales are given the values $\tau_{conv} = 12$ h, $\tau_s = \tau_c = 7$ days. Here and elsewhere, the mean sounding is taken as a radiative–convective equilibrium (RCE) in the multicloud model with parameters $\bar{\theta}_{eb} - \bar{\theta}_{em}$ and $\theta_{eb}^* - \bar{\theta}_{eb}$ as the input (31, 34). Fig. 1 reports the results of linear stability analysis for this basic state (31, 34). There is planetary-scale instability over the eight wavelengths spanning from 20,000 km to 5,000 km with dimensional intraseasonal growth rates of (30 days)$^{-1}$, intraseasonal frequencies of (20–30 days)$^{-1}$, and phase velocities in the range 2–8 m·s$^{-1}$; the most unstable wavelengths are wavenumbers 3, 4, 5, and 2 (in order of decreasing growth rate), where wavenumbers 2 and 3 have phase velocities of 6.9 and 5.8 m·s$^{-1}$, respectively. Also depicted in Fig. 1, the linearized structure of the unstable wave with wavenumber 3 shows anomalies of low-level moistening, boundary layer equivalent potential temperature $\theta_{eb}$, and congestus heating $H_c$ leading the deep convection $P$, with stratiform heating $H_s$ trailing. The unstable wave has a westward, tilted vertical structure for heating, velocity, and temperature, with clear first and second baroclinic mode contributions and with low-level cooler potential temperature lead-

**Table 2. Behavior of the MJO analog wave as the climatological parameters $\bar{Q}$ and $\bar{\theta}_{eb} - \bar{\theta}_{em}$ are varied**

| $\bar{Q}$ | $\bar{\theta}_{eb} - \bar{\theta}_{em}$, K | $k$ for which $\Gamma(k) > 0$ | $k*$ | $\Gamma(k*)$, day$^{-1}$ | $\lvert c_p(k*)\rvert$, m·s$^{-1}$ | $\Gamma(k = 2)$, day$^{-1}$ | $\lvert c_p(k = 2)\rvert$, m·s$^{-1}$ | $k_{nl}$ | $\lvert c_{nl}\rvert$, m·s$^{-1}$ |
|---|---|---|---|---|---|---|---|---|---|
| 1.0 | 11 | 2–12 | 4 | 0.042 | 5.0 | 0.028 | 6.8 | 2 | 5.6 |
| 1.0 | 12 | 2–9 | 3 | 0.034 | 5.8 | 0.025 | 6.9 | 2 | 6.1 |
| 1.0 | 14 | 2–5 | 3 | 0.018 | 5.8 | 0.016 | 7.1 | 2 | 6.7 |
| 1.0 | 15 | 2–3 | 2 | 0.0098 | 7.2 | 0.0098 | 7.2 | 2 | 7.0 |
| 1.0 | 16 | 2 | 2 | 0.0021 | 7.3 | 0.0021 | 7.3 | — | — |
| 1.0 | 17 | None | — | <0 | — | — | — | — | — |
| 0.8 | 12 | None | — | <0 | — | — | — | — | — |
| 0.85 | 12 | 2 | 2 | 0.0054 | 7.7 | 0.0054 | 7.7 | — | — |
| 0.9 | 12 | 2–3 | 2 | 0.012 | 7.4 | 0.012 | 7.4 | 2 | 7.5 |
| 0.95 | 12 | 2–5 | 3 | 0.023 | 6.0 | 0.019 | 7.2 | 2 | 6.5 |
| 1.0 | 12 | 2–9 | 3 | 0.034 | 5.8 | 0.025 | 6.9 | 2 | 6.1 |
| 1.05 | 12 | ≥2 | 4 | 0.049 | 4.7 | 0.031 | 6.6 | — | — |

The linear growth rate and phase speed at wavenumber $k$ are denoted $\Gamma(k)$ and $c_p(k)$, respectively, and the wavenumber of the maximum growth rate is $k*$. The wavenumber and phase speed of the simulated nonlinear wave are denoted $k_{nl}$ and $c_{nl}$, respectively. —, not applicable.

ing and within the deep convection. All of these features are present in the MJO (7, 23). Thus, the requirements from linear theory listed in Eq. **3** are satisfied for this regime. Next, we discuss nonlinear simulations with these parameters.

A small-amplitude symmetric perturbation of the first baroclinic velocity field is added to the basic RCE, and, by monitoring the bulk domain-averaged quantities (32), a statistical steady state is achieved by $t = 700$ days. To illustrate the resulting statistical steady state from $t = 800$–1,500 days, consider the contour plots of deep convective heating $P(x, t)$ in Fig. 2. The main feature of this figure is a wavenumber-2 wave moving eastward at 6.1 m·s$^{-1}$. This phase speed agrees well with the phase speed of 6.9 m·s$^{-1}$ predicted from linear theory for wavenumber 2. There is overall a distinct intraseasonal propagating envelope in the active and inactive phases of deep convection. Within the envelope of this wave are intense smaller-scale fluctuations moving westward. The fluctuations occur irregularly, and there are often long breaks between intense deep convective events. These features also are characteristic of the MJO (7).

The wave in Fig. 2 moves eastward rather than westward for random reasons. Because the model here has no rotation, there are both eastward- and westward-propagating unstable waves shown in Fig. 1, and one might expect to sometimes see a standing wave pattern. For a discussion of the competition between propagating and standing waves, see supporting information (SI) *Text*.

Fig. 3 shows averages from $t = 1,000$–1,500 days in a reference frame moving with the wave at 6.1 m·s$^{-1}$, which provides an effective low-frequency filter on the wave. These averages show the same progression that was seen in the linear wave: congestus heating leads deep convective heating, which, in turn, leads stratiform heating.

The velocity field (see Eq. **7**) of the wave average is shown in Fig. 4. Note the tilted structure with easterlies at low levels to the east of the deep convective heating and at higher levels to the west of the deep convective heating. Also note the strong low-level westerlies just west of the deep convective heating; this structure resembles the westerly wind burst that accompanies an MJO event (7, 23).

To summarize, there is an MJO analog wave with wavenumber 2 satisfying all of the requirements in Eq. **2** within the multicloud model; furthermore, the phase speed of this wave is predicted well by linear theory. For more discussion of this standard MJO analog wave, see *SI Text* and SI Figs. 5–10.

**The MJO Analog with Varying Climatological Parameters.** Here we study the behavior of the MJO analog wave as the climatological

parameters $\bar{Q}$ and $\bar{\theta}_{eb} - \bar{\theta}_{em}$ are varied with the remaining parameters in the multicloud model fixed. Increasing $\bar{\theta}_{eb} - \bar{\theta}_{em}$ yields a mean climatology with a relatively drier middle troposphere, and decreasing $\bar{Q}$ weakens the mean moisture gradient. Intuitively both of these effects should reduce the growth rate and the band of unstable wavenumbers. Table 2 contains a summary of the linear stability analysis about the varying climatological mean state, which confirms this intuition. In particular, as $\bar{\theta}_{eb} - \bar{\theta}_{em}$ increases through the values 15, 16, and 17 K, the number of unstable modes decreases from 2 to 1 to 0 and remains concentrated on the largest wavenumbers $k = 2, 3$ with diminishing growth rate. Similar behavior from linear theory occurs as $\bar{Q}$ is decreased in the range $1.0 \geq \bar{Q} \geq 0.8$. As reported in Table 2, if $\bar{Q}$ is increased to 1.05 with $\bar{\theta}_{eb} - \bar{\theta}_{em} = 12$ K, then all wavenumbers become unstable with growth rate constant at small scales; however, the largest growth rates, even in this situation, occur on the planetary scales. Note that even this extreme limit behavior is not what happens with the catastrophic instability of wave-CISK (conditional instability of the second kind) at small scales.

By following the same procedure as in the standard example above, numerical simulations were carried out for a wide range of the parameters reported in Table 2. In all cases, a wavenumber-2 traveling wave that is an MJO analog emerged in the statistical steady state with a speed in the range 5–8 m·s$^{-1}$; furthermore, as indicated in Table 2, linear theory provides an excellent estimate for this wave speed.

As the climatological parameters vary, the intensity of the wave fluctuations within the propagating envelope changes dramatically. This result, and other results, are shown in *SI Text*, SI Figs. 11–17, and SI Table 3. Among other things in *SI Text*, there are discussions of the effects of varying $\tau_s$, $\tau_c$, and $\tau_{conv}$; imposing a spatially varying sea surface temperature; and adding a uniform easterly barotropic mean wind.

**Concluding Discussion**

An MJO analog model with all of the features in Eq. **2** has been developed here by using a recent multicloud model (31–34) with intraseasonal time scales for the multicloud dynamics in Eq. **1**. The only nonlinearities in the model as listed in Eq. **4** are low-level moisture advection and convective switches so that other mechanisms, such as those listed below Eq. **4**, are completely absent. Nevertheless, the results reported in Figs. 2–4 show qualitative fidelity with key features of the observational record in the zonal direction of the actual MJO (7, 23). The analog MJO waves move at speeds of 5–7 m·s$^{-1}$, and linear instability theory successfully predicts their phase speed. With all

this behavior mentioned above in the multicloud model and the intense current interest in predicting intraseasonal variability in the Tropics (6), the MJO analog models discussed here should be useful for intraseasonal predictability studies in a fashion akin to the Lorenz 96 model (39) for the midlatitude atmosphere.

A major future direction is to include the effects of rotation in the present MJO analog models, because this is a likely source of the MJO's eastward-propagation direction. There is a systematic route to do this for linear theory (40). The next step is to do nonlinear simulations in such a model and then systematically add important physical effects, such as upscale eddy fluxes of momentum and temperature, active boundary layer dynamics, and radiation to the present models, to improve their fidelity with the observational record for the MJO. Because the westerly wind burst in the present models is relatively weak, one can anticipate that upscale transport of momentum might be especially significant in a more complex model with rotation.

1. Madden RA, Julian PR (1972) *J Atmos Sci* 29:1109–1123.
2. Nakazawa T (1988) *J Met Soc Jpn* 66:823–839.
3. Hendon HH, Salby ML (1994) *J Atmos Sci* 51:2225–2237.
4. Hendon HH, Liebmann B (1994) *J Geophys Res* 99:8073–8084.
5. Maloney ED, Hartmann DL (1998) *J Climate* 11:2387–2403.
6. Lau WKM, Waliser DE, eds (2005) *Intraseasonal Variability in the Atmosphere-Ocean Climate System* (Springer, Berlin).
7. Zhang C (2005) *Rev Geophys* 43:G2003+.
8. Sperber KR, Slingo JM, Inness PM, Lau WK-M (1997) *Climate Dyn* 13:769–795.
9. Lin J-L, Kiladis GN, Mapes BE, Weickmann KM, Sperber KR, Lin W, Wheeler M, Schubert SD, Del Genio A, Donner LJ, *et al.* (2006) *J Climate* 19:2665–2690.
10. Emanuel KA (1987) *J Atmos Sci* 44:2324–2340.
11. Neelin JD, Held IM, Cook KH (1987) *J Atmos Sci* 44:2341–2348.
12. Wang B, Rui H (1990) *J Atmos Sci* 47:397–413.
13. Salby ML, Garcia RR, Hendon HH (1994) *J Atmos Sci* 51:2344–2367.
14. Raymond DJ (2001) *J Atmos Sci* 58:2807–2819.
15. Chao WC (1987) *J Atmos Sci* 44:1940–1949.
16. Moncrieff MW (2004) *J Atmos Sci* 61:1521–1538.
17. Grabowski WW (2001) *J Atmos Sci* 58:978–997.
18. Grabowski WW (2003) *J Atmos Sci* 60:847–864.
19. Majda AJ, Biello JA (2004) *Proc Nat Acad Sci USA* 101:4736–4741.
20. Biello JA, Majda AJ (2005) *J Atmos Sci* 62:1694–1721.
21. Biello JA, Majda AJ (2006) *Dyn Atmos Oceans* 42:152–215.
22. Johnson RH, Rickenbach TM, Rutledge SA, Ciesielski PE, Schubert WH (1999) *J Climate* 12:2397–2418.
23. Lin X, Johnson RH (1996) *J Atmos Sci* 53:695–715.
24. Yanai M, Chen B, Tung W-W (2000) *J Atmos Sci* 57:2374–2396.
25. Houze RA, Jr, Chen SS, Kingsmill DE, Serra Y, Yuter SE (2000) *J Atmos Sci* 57:3058–3089.
26. Straub KH, Kiladis GN (2002) *J Atmos Sci* 59:30–53.
27. Haertel PT, Kiladis GN (2004) *J Atmos Sci* 61:2707–2721.
28. Kiladis GN, Straub KH, Haertel PT (2005) *J Atmos Sci* 62:2790–2809.
29. Mapes BE (2000) *J Atmos Sci* 57:1515–1535.
30. Majda AJ, Shefter MG (2001) *J Atmos Sci* 58:1567–1584.
31. Khouider B, Majda AJ (2006) *J Atmos Sci* 63:1308–1323.
32. Khouider B, Majda AJ (2007) *J Atmos Sci* 64:381–400.
33. Khouider B, Majda AJ (2006) *Dyn Atmos Oceans* 42:59–80.
34. Khouider B, Majda AJ (2006) *Theor Comp Fluid Dyn* 20:351–375.
35. Wheeler M, Kiladis GN (1999) *J Atmos Sci* 56:374–399.
36. Wheeler M, Kiladis GN, Webster PJ (2000) *J Atmos Sci* 57:613–640.
37. Mapes BE, Tulich S, Lin J-L, Zuidema P (2006) *Dyn Atmos Oceans* 42:3–29.
38. Bretherton CS, Peters ME, Back LE (2004) *J Clim* 15:2907–2920.
39. Lorenz EN, Emanuel KA (1998) *J Atmos Sci* 55:399–414.
40. Majda AJ, Khouider B, Kiladis GN, Straub KH, Shefter MG (2004) *J Atmos Sci* 61:2188–2205.